Anita A. Dey, Yahya Modarres-Sadeghi, Jonathan P. Rothstein

Department of Mechanical and Industrial Engineering, University of Massachusetts, Amherst, Massachusetts 01003, USA

Abstract

Under the right conditions, viscoelastic fluids can exhibit elastic flow instabilities in the absence of inertia. If the fluid is in contact with a flexible or flexibly-mounted structure, these elastic flow instabilities lead to time-dependent forces on the structure, which can cause the structure to oscillate. This constitutes a new class of Viscoelastic Fluid-Structure Interactions (VFSI). Up until now, the VFSI reported in the literature demonstrated a oneway coupling between the fluid and the structure where little feedback from the structure to the flow was observed. Here, we report for the very first time, the presence of a lockin behaviour in VFSI. We have designed and conducted a set of experiments in which the frequency of the elastic flow instabilities and the natural frequency of the flexible structure become equal as the flow velocity is increased, and therefore lock-in is observed. We present amplitude and frequency responses of two sets of flexibly-mounted cylinders over a range of Weissenberg numbers and reduced velocities to show the lock-in range. The time-varying flow fields inside and outside the lock-in range were studied through streak-line imaging and particle image velocimetry. The viscoelastic lock-in range was observed for a Weissenberg number range of $5 \le Wi \le 15$ for one of the cylinders tested and for a range of $20 \le Wi \le 30$ for the other. For both cylinders, the lock-in started at a reduced velocity of $V_r \approx 1.5$. In Cylinder 1, the lock-in ended at $V_r \approx 4$, while for Cylinder 2 the end of the lock-in was not observed, because the data points did not cover a wide enough range. Similar to the lock-in observed in the typical VIV response in a Newtonian fluid, the frequency of the elastic flow instability was found to increase with increasing flow velocity before plateauing at the natural frequency of the cylinder in the lock-in range. Unlike the VIV response of a Newtonian fluid, where the lock-in range corresponds to the maximum observed amplitude of oscillations, in VFSI the amplitude of oscillations reached a plateau while in lock-in, but increased with Weissenberg number and reduced velocity before and after the lock-in range.

1. Introduction

Vortex-Induced Vibrations (VIV) is a canonical problem in Fluid-Structure Interactions (FSI) and has been studied extensively [2, 29, 31]. In a classical VIV problem, a flexibly-mounted cylinder is placed in a Newtonian fluid flow, and it is free to oscillate in a direction perpendicular to the direction of the incoming flow (the crossflow direction). At a reduced

Email address: rothstein@ecs.umass.edu (Jonathan P. Rothstein)

velocity of approximately $V_r = 5$ (defined as $V_r = U/f_nD$, where U is the incoming flow velocity, f_n is the structure's natural frequency, and D is the cylinder's diameter), the shedding frequency and the structure's natural frequency become equal, resulting in relatively-large amplitude oscillations over a range of reduced velocities. This range, in which the shedding frequency and the frequency of oscillations stay equal, is called the lock-in range. Lock-in also exists in cases where the cylinder is free to oscillate in the direction of flow (the inline direction), in which case two separate ranges of non-zero amplitude oscillations, corresponding to two different types of lock-in are observed [15, 6, 4, 5, 7]. In the first lock-in range, starting at $V_r \approx 1.7$, the cylinder's oscillations is synchronized with a symmetric shedding of vortices, and in the second lock-in range, starting at $V_r \approx 2.5$, the cylinder's oscillations are synchronized with an asymmetric shedding of vortices. A cylinder free to oscillate both in the crossflow and inline directions can also experience lock-in in both directions simultaneously, resulting in responses with figure-eight orbits [9].

Very recent studies have shown evidence of fluid-structure interactions in systems where the fluid is viscoelastic [10, 11, 12, 16, 17]. Viscoelastic fluids have been shown to exhibit purely elastic flow instabilities at vanishingly small Reynolds numbers and large Weissenberg numbers [30, 23, 21, 14]. In the recent studies on FSI in systems with viscoelastic fluid, it has been shown that when the elastic instabilities occur close to a flexible structure, the flow forces that act on the structure cause it to respond, and structural oscillations are observed [10, 11, 12, 16, 17]. However, in none of the previous VFSI studies has lock-in been observed. In these previous studies, the frequency of the elastic flow instabilities has always been much smaller than the structural natural frequency. The frequency of the elastic flow instabilities defines the frequency of the external fluctuating force that acts on the structure (similar to the shedding frequency in a typical VIV response), and if it is much smaller than the natural frequency of the system, it will not be possible to observe any lock-in. The frequency of the elastic flow instability, f, is inversely proportional to the fluid's relaxation time, λ , and the typical values for the fluid relaxation time studied in the VFSI experiments in the literature have been on the order of $\lambda > 10$ s. Therefore, a structural natural frequency of $f_N \approx 0.1$ Hz [12, 16] would have been needed to observe lock-in. In the previous VFSI studies, the natural frequencies were significantly larger than 0.1 Hz, making it impossible to observe lock-in. In this paper, we bring these two frequencies closer to each other by tuning the structural property and fluid rheology, in order to make the lock-in behavior possible for the very first time in a VFSI study.

The viscoelastic fluid used in this study is a wormlike micelle solution. These solutions are composed of surfactant molecules with a hydrophilic head and a hydrophobic tail. Beyond a critical micelle concentration (CMC), the surfactant molecules will self-assemble to form larger and complex shapes such as spherical and wormlike micelles as a mechanism to minimize the exposure of their hydrophobic tails to water [18, 22, 27]. With increasing concentration, the entangled wormlike micelles, although physically different from polymers, can display similar viscoelastic properties. Additionally, wormlike micelles can relieve stress through breaking and reforming [27] or by creating a temporary branch point to allow two entangled micelles to pull through each other in what is known as a 'ghost-like' crossing [19]. These wormlike micelle solutions can exhibit strong shear thinning [27] and strain hardening of their extensional viscosity [28]. In extensional flows like those imposed by a filament stretching extensional rheometer, these wormlike micelle solutions undergo a dramatic fail-

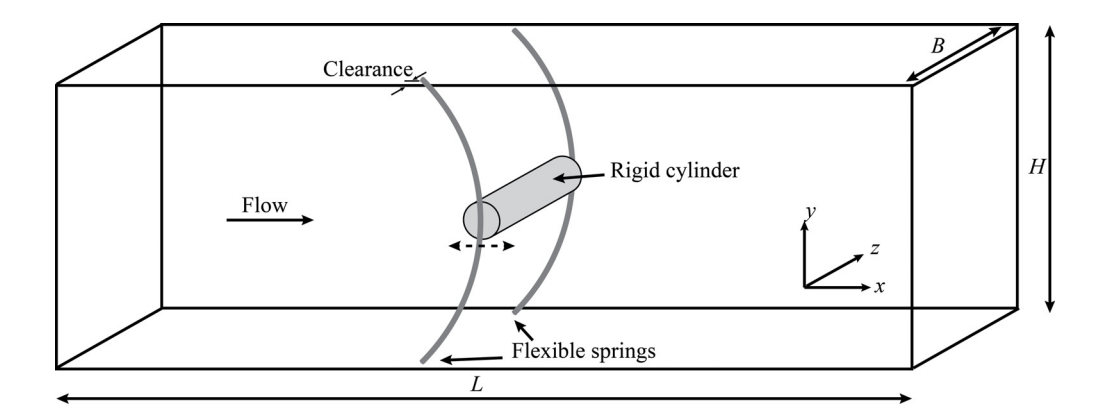


Figure 1: Schematic diagram of the rigid cylinder supported by flexible springs and allowed to oscillate in the inline direction when placed in a viscoelastic fluid flow. The dashed double arrowhead denotes the plane of the flow-induced cylinder oscillations.

ure near the filament mid-plane which is believed to be due to the scission of individual micelle chains [3]. Wormlike micelle scission has also been observed in flows with complex kinematics like flows past spheres and cylinders [26, 8, 25, 13, 24]. In each case, the flow becomes unstable and undergoes elastic instabilities due to a breakdown in the micellar network in the extensional flow, localized to within the wake of the sphere or the cylinder. It is this flow-induced micelle scission that leads to VFSI of elastic sheets and flexible cylinders [11, 12].

This paper describes the investigation of the existence and mechanism of a lock-in between the flow of a viscoelastic wormlike micelle solution and a flexibly-mounted cylinder over a wide range of Weissenberg numbers. A rigid cylinder was supported by flexible springs with an easily tunable frequency due to the tension imposed in the springs. The use of a rigid cylinder eliminated a complex lengthwise deformation, previously seen in a flexible cylinder placed in a wormlike micelle solution [12] and also maintained a single degree of freedom in the inline direction. This direction was chosen for the degree of freedom, because previous VFSI studies with a flexible cylinder, free to oscillate in the crossflow and inline directions [12], showed oscillations mainly in the inline direction.

In order to bring the frequency of the onset of elastic flow instabilities closer to the structural natural frequency, the rheology of the wormlike micelle solution was formulated to have a relaxation time whose inverse was comparable to the natural frequency of the flexibly-mounted cylinder. The interactions of the elastic flow instabilities with the flexibly-mounted cylinder are presented here for cylinders with two different natural frequencies. The phenomenon of lock-in in VFSI, the characteristics of the flow field inside and outside the lock-in range, and the fundamental distinctions from lock-in in Newtonian FSI are discussed in detail.

2. Experimental setup

Fig. 1 is a schematic diagram of the experimental setup used in this study. A rigid acrylic cylinder supported by flexible springs was placed at the center of a rectangular channel with a length of L=450 mm and breadth and height of B=H=50 mm. The diameter and the

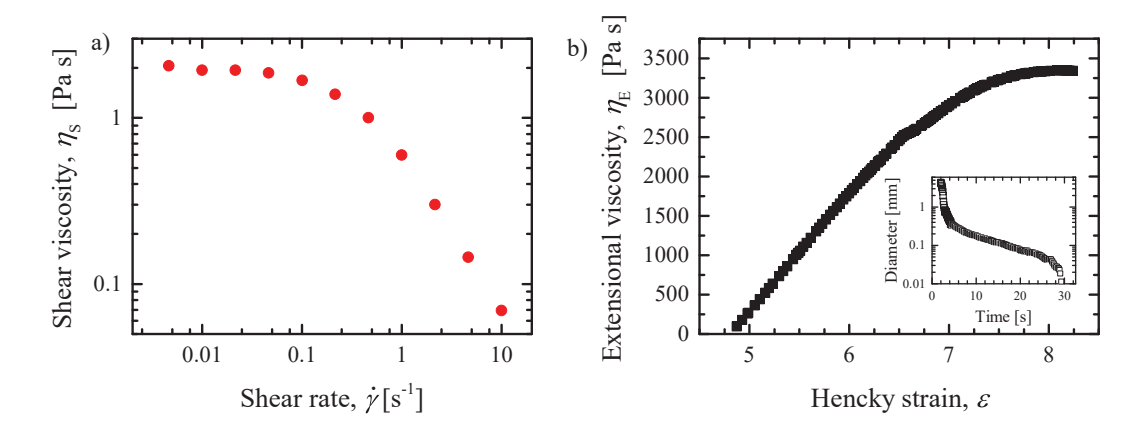


Figure 2: (a) Shear viscosity as a function of the shear rate and (b) the extensional viscosity versus Hencky strain of the viscoelastic wormlike micelle solution. The inset is a representative plot of the exponential decay of the diameter with time.

aspect ratio (L/D) of the acrylic cylinder were D=6.3 mm and L/D=7.5, respectively while those of the flexible spring were d = 1.2 mm and L/d = 41.7, respectively. The flexible springs were fabricated from polydimethysiloxane (PDMS) using a 40:1 volume ratio of the base and curing agent from a Sylgard-184 silicone elastomer kit (Dow Corning) resulting in an elastic modulus of E=0.5 MPa and a spring constant of k=11.3 N/m. The PDMS mixture was first de-gassed in a vacuum chamber and then carefully filled into glass capillary tubes which served as the molds for the cylindrical springs. The PDMS-filled glass tubes were then left to cure for 24 hours. After curing, the thin glass tubes were cracked open to release the flexible spring inside. The fabricated flexible springs were first attached to the rigid cylinder and then sealed into the through-holes drilled into the top and bottom walls of the flow cell leaving a clearance space of 0.5 mm from the side walls. A fast-curing 5:1 volume ratio of the base from the Sylgard-184 kit and 25-30% methylhydrosiloxanedimethylsiloxane copolymer (HMS-301 Gelest Inc.) was used as the sealing agent. The Weissenberg number for the flow past the flexible springs was found to be a factor of 4 smaller than the Weissenberg number around the cylinder. As a result, the flow around the flexible springs remained stable and did not affect the results. The natural frequency of the flexibly-mounted cylinder was tuned by adjusting the tension in the flexible springs before sealing their other end. Cylinders with two different natural frequencies were tested. Cylinder 1 had a natural frequency of $f_{N1} = 1$ Hz and Cylinder 2 had a natural frequency of $f_{N2}=3$ Hz. The elastic modulus of the springs was tested on the Instron and the linear range was found to extend well past the strains experienced in the experiments.

A wormlike micelle solution composed of 5 mM of cationic surfactant cetyltrimethylammoniun bromide (CTAB) (MP Biomedicals) and 5 mM of sodium salicylate (NaSal) (Fisher Scientific) in deionized water was employed as the viscoelastic test fluid. At this concentration, the solution is above the critical micelle concentration (CMC) which, for CTAB in pure water is CMC = 0.9 mM and lowers in the presence of salt [18]. The surfactant and salt were dissolved in water using a magnetic stirrer and then allowed to rest for 24 hours before the start of experiments. The shear rheology of the fluid, shown in Fig. 2(a), was measured using a stress-controlled rheometer (TA instruments, AR2000) with a 6 cm plate diameter and 2°

cone geometry. The zero shear viscosity was found to be $\eta_0 = 2$ Pa-s and with increasing shear rate, the fluid began to shear-thin heavily, with a slope of $\eta \propto \dot{\gamma}^{-0.88}$. Using a capillary breakup extensional rheometer (CaBER), the fluid relaxation time was measured to be $\lambda = 4$ s. A steady-state extensional viscosity of $\eta_E = 3300$ Pa-s was also measured using this method [1]. The strain-hardening behaviour of this fluid can be observed in Fig. 2(b). With the theoretical limit for the Trouton ratio of a Newtonian fluid being $Tr = \eta_E/\eta_0 = 3$, the final Trouton ratio for this wormlike micelle solution was found to be significantly larger at Tr = 1650.

The flow was controlled by a positive displacement pump driven by a linear motor to minimize any pressure fluctuations [25]. The flow velocity was varied from 0 to 50 mm/s during the study. The motion of the flexibly-mounted cylinder was captured at 100 frames per second using a high speed camera (Phantom V4.2). The recorded displacement of the cylinder was then digitized using a tracking software (Tracker) which had an uncertainty of ± 0.1 mm. The flow field behaviour during the fluid-structure interactions was studied using the Particle Image Velocimetry technique. The viscoelastic fluid was seeded with silver coated glass spheres (Spheriglass, Potters Industries) at 0.005% by weight, and allowed to equilibrate in the fluid for 24 hours. During experiments, the flow field was illuminated by a laser light sheet formed by passing a 500 mW argon laser (National Laser 458 – 514 nm) through a cylindrical lens. The motion of the illuminated spheres was recorded using a high-speed camera (Vision Research VEO 640L) at a frame rate of 400 frames per second and processed in a commercial PIV software (LaVision). Long-exposure streakline images were also processed from these videos using ImageJ (NIH).

3. Results

3.1. Amplitude and frequency of the response

The viscoelastic flow past a flexibly-mounted cylinder was studied for two different structural natural frequencies. Cylinder 1 had a natural frequency of $f_{N1} = 1$ Hz and Cylinder 2 had a natural frequency of $f_{N2} = 3$ Hz. The natural frequencies were obtained through pluck tests conducted on the cylinders when immersed in the viscoelastic fluid under zero-flow conditions. The mass ratio, the ratio of cylinder mass to displaced fluid mass, was measured to be $m^* = 1.5$. In the left plots of Fig. 3, the non-dimensional oscillation amplitude and frequency of the two flexibly-mounted cylinders have been plotted as a function of the Weissenberg number. The Weissenberg number describes the relative importance of elasticity to the viscosity in a flow and is defined as $Wi = \lambda U/D$, where λ is the fluid relaxation time, U is the flow velocity and D is the cylinder diameter. The non-dimensional oscillation amplitude and frequency are defined as $A^* = A/D$ and $f^* = f/f_N$, respectively. The standard deviation was calculated from 4 repeated experiments, each comprising of at least 10 oscillation cycles in a single experiment run.

Beyond a critical Weissenberg number of $Wi_{crit} = 5.5$, the flow became unstable for both Cylinders 1 and 2 and both cylinders started to oscillate. The initial oscillation frequencies of Cylinder 1 and Cylinder 2 were $f_1 = 0.5$ Hz and $f_2 = 0.14$ Hz, respectively. The mechanism of the flow instability driving these oscillations was similar to those reported for the unstable flow of wormlike micelle solutions past a flexible cylinder and a flexible sheet [11, 12]. Specifically, elastic stresses are built up in the wake of the cylinder where a strong extensional flow

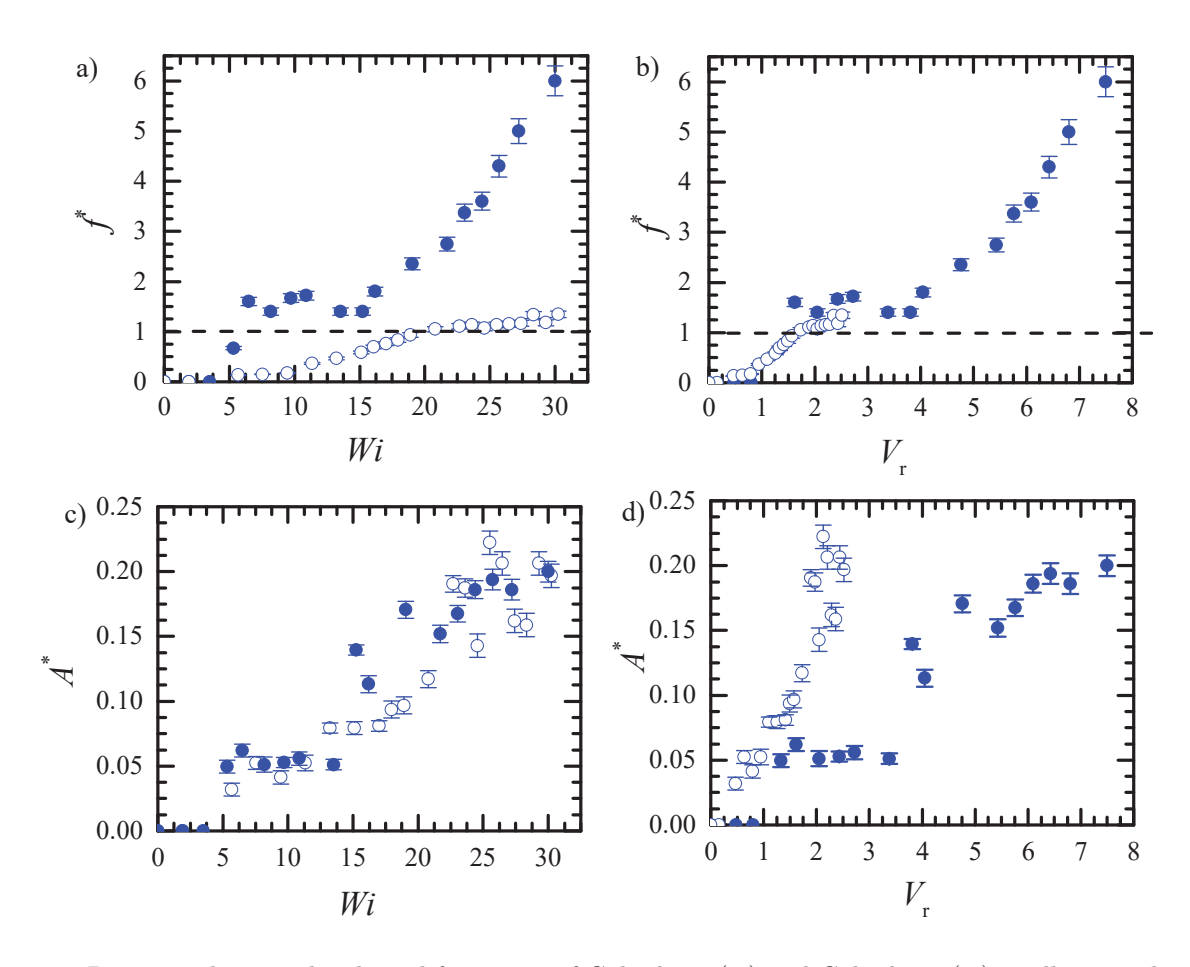


Figure 3: Dimensionless amplitude and frequency of Cylinder 1 (\bullet) and Cylinder 2 (\bigcirc) oscillations plotted as a function of the (a,c) Weissenberg number and the (b,d) reduced velocity. The error bars denote the standard deviation observed in 4 repeated experiments, each comprising of at least 10 oscillation cycles in a single experiment run.

is present. When this stress grows beyond the cohesive strength of the wormlike micelles in solution, they have been observed through flow-induced birefringence measurements to fail and breakdown into smaller less-elastic micelles. At that moment, the elastic stresses in the wake are released and the cylinder quickly recoils back upstream. As new, fresh fluid is swept into the wake, the elastic stresses grow again, and the cycle repeats. For Cylinder 1, the non-dimensional frequency of oscillations increased initially and reached a plateau at $f^* = 1.5$ over a range of Weissenberg numbers of 6.5 < Wi < 16. For Wi > 16, the frequency of oscillations increased monotonically again with Weissenberg number. The amplitude of oscillations initially increased linearly with Weissenberg number, however, during lock-in, the amplitude of oscillations remained constant at $A^* \approx 0.05$, before increasing monotonically again at Weissenberg numbers beyond the lock-in range. From the error bars superimposed over the data in Fig. 3(c), it is clear that this plateau in the oscillation amplitude during lock-in is significant. The fact that the amplitude of oscillations increases monotonically before and after the lock-in range is different from the case of Newtonian flows, in which oscillations are observed only in the lock-in range.

In the case of Cylinder 2, the cylinder oscillation frequency increased with the Weissenberg number until reaching a plateau at $f^* = 1.1$ for a Weissenberg number range of 20 < Wi < 30. Due to the maximum obtainable flow rate of our pumps, we could not obtain data for Cylinder 2 beyond Wi > 30. As a result, a complete picture of the lock in range is not available for this case. Similar to the case of Cylinder 1, initially the oscillation amplitude of Cylinder 2 increased monotonically with the Weissenberg number for Wi < 20 (Fig. 3(c)). Within the lock-in range, 20 < Wi < 30, the amplitude growth transitioned to a plateau at $A^* \approx 0.2$, although some fluctuations in the amplitude were observed in this range.

If the amplitude and frequency results are plotted versus the reduced velocity, as is usually done in plotting the results of Newtonian VIV, the lock-in range for both cylinders start at an approximately the same reduced velocity, as observed in Fig. 3(b,d). The frequency plot shows an initial increase in the frequency with increasing reduced velocity, but at a reduced velocity of $V_r \approx 1.5$ for both cases, there is a sudden change in the slope of the frequency plot and the frequency ratio remains constant over a range of reduced velocities. This is clear for the case of Cylinder 1, where the entire lock-in range is observed over a reduced velocities range of $1.5 < V_r < 4$. Curiously enough, this range of reduced velocities is the same as the range of reduced velocities for which VIV is observed for a one degree of freedom (1 DOF) cylinder free to oscillate in the inline direction and placed in Newtonian flow [15]. For the Newtonian case, two ranges of oscillations are observed separated by a range of almost-zero amplitude oscillations in between them. Clearly, the mechanisms responsible for the cylinder excitation in these two cases are quite different, but the similarity of the lock-in ranges seem interesting, although perhaps coincidental. For Cylinder 2, the lock-in starts at approximately the same value as for Cylinder 1, but our data end soon after the lock-in starts, and therefore a complete image of the lock-in for Cylinder 2 is not available. However, the beginning of the lock-in has been clearly captured with the initial data points. The amplitude of oscillations for the lock-in that is observed in Cylinder 2 is much larger than the amplitude of oscillations in the lock-in range for Cylinder 1 ($A^* = 0.2$ versus $A^* = 0.05$.) because the onset of lock-in for Cylinder 2 is at a much higher Weissenberg number than that for Cylinder 1. Outside the lock-in ranges, the amplitude of oscillations grows linearly with increasing Weissenberg number, and if the lock-in starts at a higher Weissenberg number, its

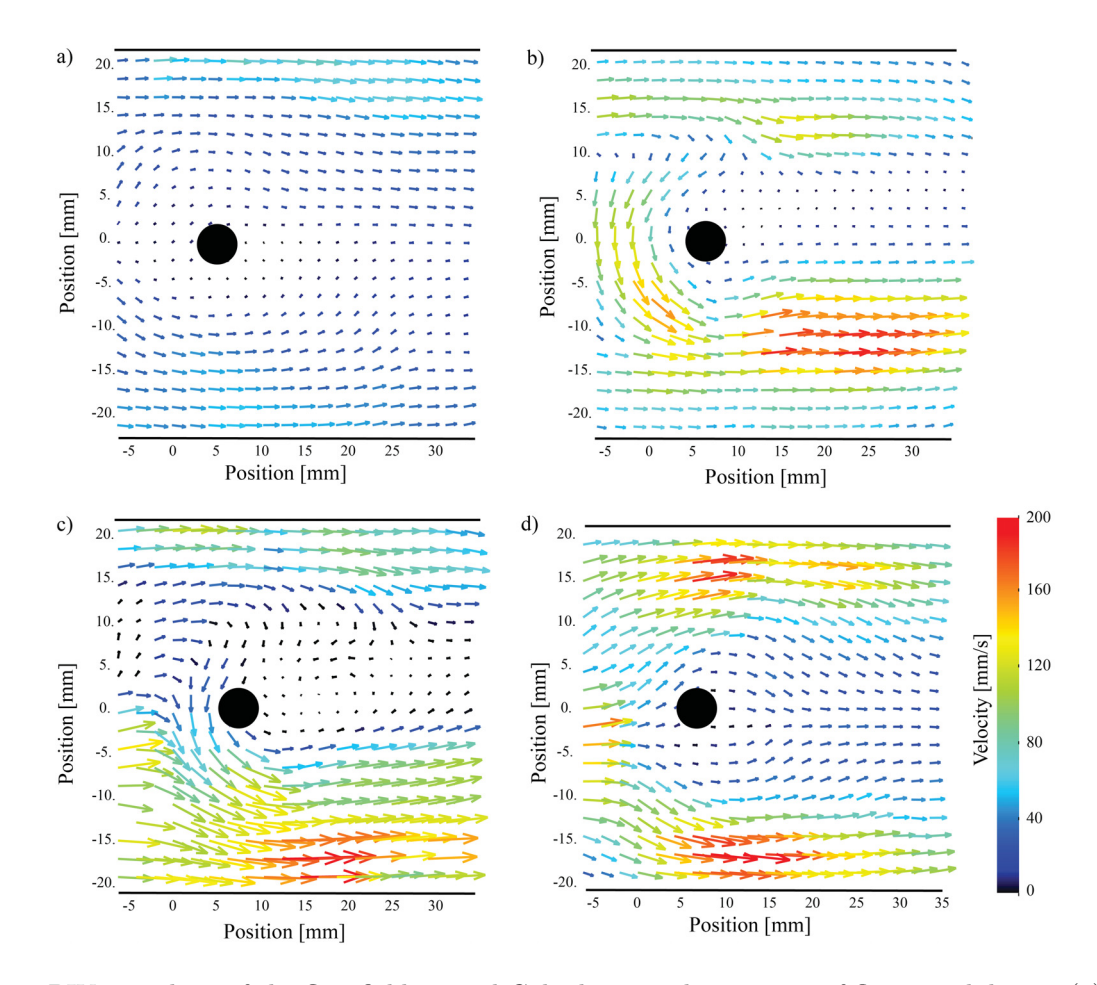


Figure 4: PIV snapshots of the flow field around Cylinder 1 at the instance of flow instability at (a) $Wi = 3.5, V_r = 0.8$, (b) $Wi = 5, V_r = 1.3$, (c) $Wi = 10, V_r = 2.5$ and (d) $Wi = 24, V_r = 6$. For the cases in (b-d) the flow is unstable and these PIV vector fields represent a point near the maximum displacement of the cylinder just following the onset of the elastic instability.

corresponding amplitude of oscillations will be larger. Note also that the frequency ratio is slightly larger than $f^* = 1$ in the lock-in range ($f_1^* \approx 1.5$ for Cylinder 1 and at $f_2^* \approx 1.1$ in the case of Cylinder 2), similar to what is observed in the Newtonian lock-in of low-mass-ratio systems [20].

3.2. Wake visualization

In order to explore the dynamic coupling between cylinder oscillations and the flow instabilities occurring in the flow field, streakline and PIV imaging were performed. In Fig. 4, PIV images are presented for the flow field around Cylinder 1 to illustrate the changes that occur in the wake of the cylinder with increasing Weissenberg number. PIV data are presented for Weissenberg numbers of Wi = 3.5, 5, 10 and 24, corresponding to reduced velocities of $V_r = 0.8, 1.3, 2.5$, and 6. For this cylinder, for Wi > 5 the flow becomes unstable. In Fig. 4(a), a stable, low Weissenberg number (Wi = 3.5) flow is shown. The flow is symmetric above and below the cylinder with a region of strong extensional flow in the cylinder wake that leads to large extensional stresses and eventually to a flow instability when the stresses surpass the cohesive strength of the micelles in the flow. The flow profile is consistent with previous measurements for flow of wormlike micelle solutions around a fixed cylinder [25].

As the Weissenberg number is increased, the flow approaching the cylinder first becomes asymmetric and then becomes unsteady (Fig. 4(b)). Even before the onset of the elastic flow instabilities, the asymmetry in these flows can become quite stark [12, 16]. In Fig. 4(b), a PIV vector field from a snapshot in time for an unstable flow right before the lock-in range at a Weissenberg number of Wi = 5 and reduced velocity of $V_r = 1.3$ is shown. These PIV vector fields are taken just after the onset of the elastic instability to highlight the point of maximum asymmetry in the flow. Complete time histories of the PIV vector fields are presented later in the text. In Fig. 4(b), the upstream stagnation point on the cylinder has moved from the centerline at $\theta = 0^{\circ}$ observed for low Weissenberg number flows to far above the centerline at an angle of approximately $\theta = -90^{\circ}$. In addition to changes to the stagnation point, the flow behavior is quite different. The flow above the cylinder initially moves past the cylinder before reversing direction, flowing back upstream towards the cylinder, crossing the upstream face of the cylinder and flowing around the cylinder to the bottom of the cylinder before continuing to flow downstream towards the outlet. This break in symmetry occurred both above and below the cylinder from one experiment to the next without preference. However, to be consistent, all cases presented here are for measurements where the flow reversal was observed above the cylinder. Similar asymmetric flow patterns were observed for the flow of a wormlike micelle solution past a flexible PDMS cylinder [12] and a flexible cantilevered glass cylinder [16]. The asymmetry in the flow field increased in intensity with increasing Weissenberg number.

In Fig. 4(c), an example of the wake structure is shown at a Weissenberg number of Wi = 10 and a reduced velocity of $V_r = 2.5$, where lock-in was observed. In this case, the asymmetric flow extends even further downstream of the cylinder and the stagnation point moves even further downstream to $\theta \approx -120^{\circ}$. A distinguishing feature of the flow in the lock-in range is the presence of a reversed flow deep in the wake of the cylinder. This can be seen in the upper right quadrant of Fig. 4(c) where reversed flow can be observed more than 15 mm, or roughly 2.5D, downstream of the cylinder. This can be contrasted to the reversed

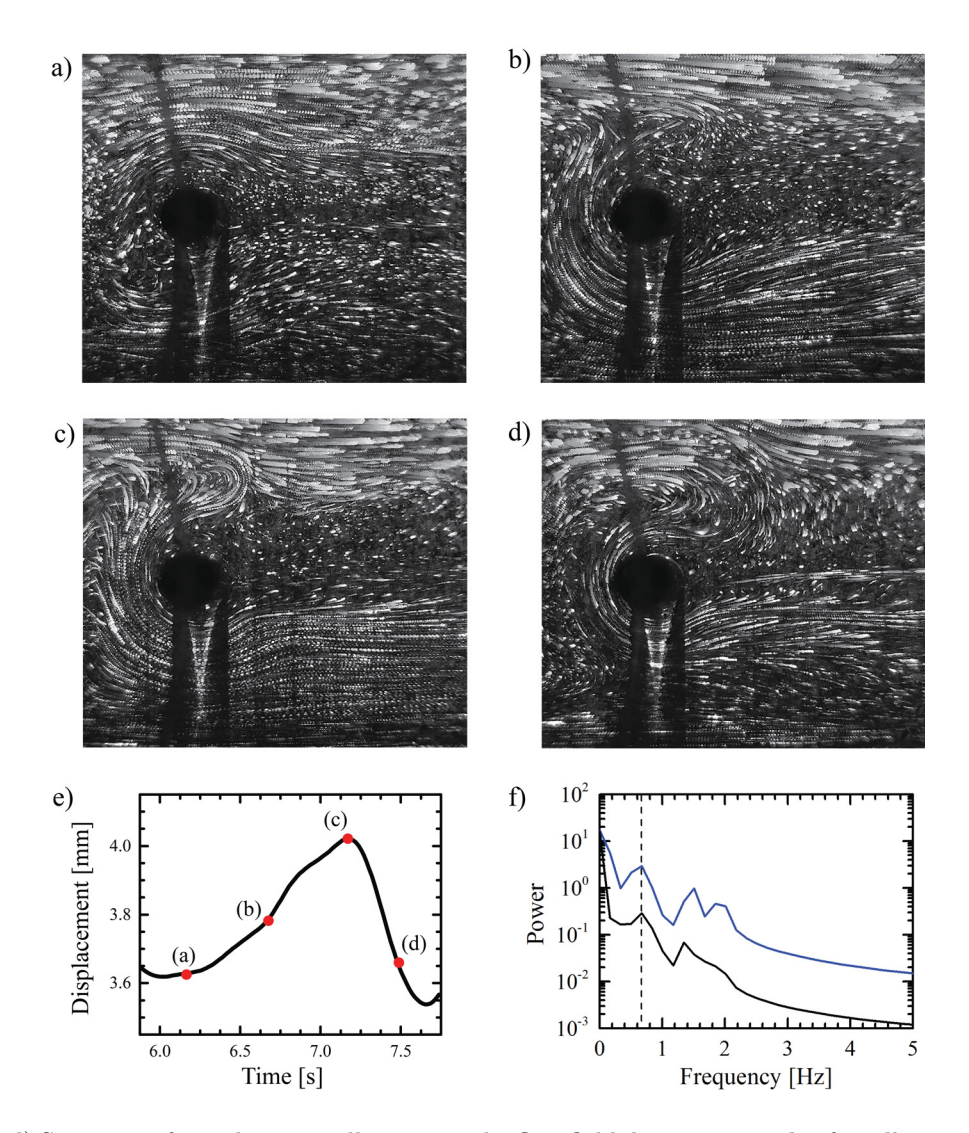


Figure 5: (a-d) Sequence of streak images illustrating the flow field during one cycle of oscillations at Wi = 3.5 and $V_r = 0.8$ for Cylinder 1. The images correspond to the time history in (e) when the cylinder starts from its minimum displacement and continues through one complete cycle of oscillations. The flow is from left to right. The time between images is 0.08 s. (f) The power spectra derived from the cylinder displacement (black) and fluctuating PIV velocity vectors (blue) located 20mm downstream in the wake of the cylinder centerline.

flow seen in Fig. 4(b), where the reversed flow was only observed beside the cylinder and not deep into its wake. This is an example of the two-way coupling that is synonymous with the lock-in behaviour observed in Newtonian FSI. Within the lock-in range, the cylinder oscillates at its natural frequency, the frequency does not continue to increase with flow rate, and the structure dominates the motion and influences the wake. The most significant flow change occurs during the recoil journey of the cylinder as a significant fluid volume is drawn with the cylinder back upstream against the oncoming flow. Note that the cylinder oscillates in the inline direction, and in the lock-in range, moves the fluid with itself in the inline direction, as it goes through its cycle of oscillations. As the Weissenberg number is increased further, the cylinder leaves the lock-in range and the heavily reversed flow disappears. Although the flow structure in Fig. 4(d) is not fully symmetric, the reversed flow is no longer present and the stagnation point has returned to close to the leading edge of the cylinder, at $\theta \approx 0^{\circ}$.

A time sequence of streakline images of the flow field occurring during the course of one cycle of oscillations of Cylinder 1 at Wi = 3.5 and $V_r = 0.8$ is shown in Fig. 5. Note that the streak images for the flow around Cylinder 2 appear nearly identical to those in Fig. 5 if they are compared at the same reduced velocity. At this Weissenberg number and reduced velocity, the frequency of oscillations is not yet within the lock-in range. In Fig. 5, the flow is asymmetric with more flow moving around the bottom of the cylinder than above. A low speed wake extends down and to the right of the cylinder as a result of the asymmetry. No flow separation is observed here, either downstream as would be expected for a high Reynolds number flow, or upstream as has been observed for some high Weissenberg number flows. The asymmetry likely stems from a combination of the high shear thinning and strong extensional thickening nature of these wormlike micelle solutions [8]. In Fig. 5(a), the flow in the lower half of the flow field beside the cylinder reversed its direction as moved upwards across the upstream face of the cylinder and over the top of the cylinder before moving downstream. With time, the flow reversal intensified and moved downstream as seen in Fig. 5(b). During the period of flow reversal growth, the static deflection of the cylinder increased by 0.5D. At the point of the maximum amplitude, Fig. 5(c), a flow instability occurred in the wake of the cylinder, visible by the formation of a jet seen in the image as bright horizontal streak in the mid-plane of the flow field. This flow instability is the result of a breakdown of wormlike micelles in the strong extensional flow in the wake of the cylinder. With the loss of a significant amount of elastic stress in the wake of the cylinder, it recoiled rapidly. Note that both the jet and the region of reversed flow disappear as the cylinder approaches its minimum deflection, and the cycle shown in Fig. 5(e) is repeated. The power spectra of the cylinder displacement and the fluctuating PIV velocity vectors located 20 mm downstream in the wake of the cylinder have been plotted against frequency in Fig. 5(f). The overlapping dominant peaks confirm that the cylinder oscillations are directly influenced by the wake instability.

In order to compare the cylinder wake in and out of the lock-in range, time sequences of PIV vector fields are presented for Cylinder 1 during one cycle of cylinder oscillations within the lock-in range in Fig. 6 at Wi = 10 and $V_r = 2.5$, and after the lock-in region in Fig. 7 at Wi = 24 and $V_r = 6$. In the lock-in range, the flow is asymmetric, with a major fraction of the fluid moving downwards around the upper half of the cylinder. The onset of instability corresponds to the formation of a jet downstream of the cylinder in its extensional wake as shown in Fig. 6(a). Before the lock-in range, the jet is weaker and the

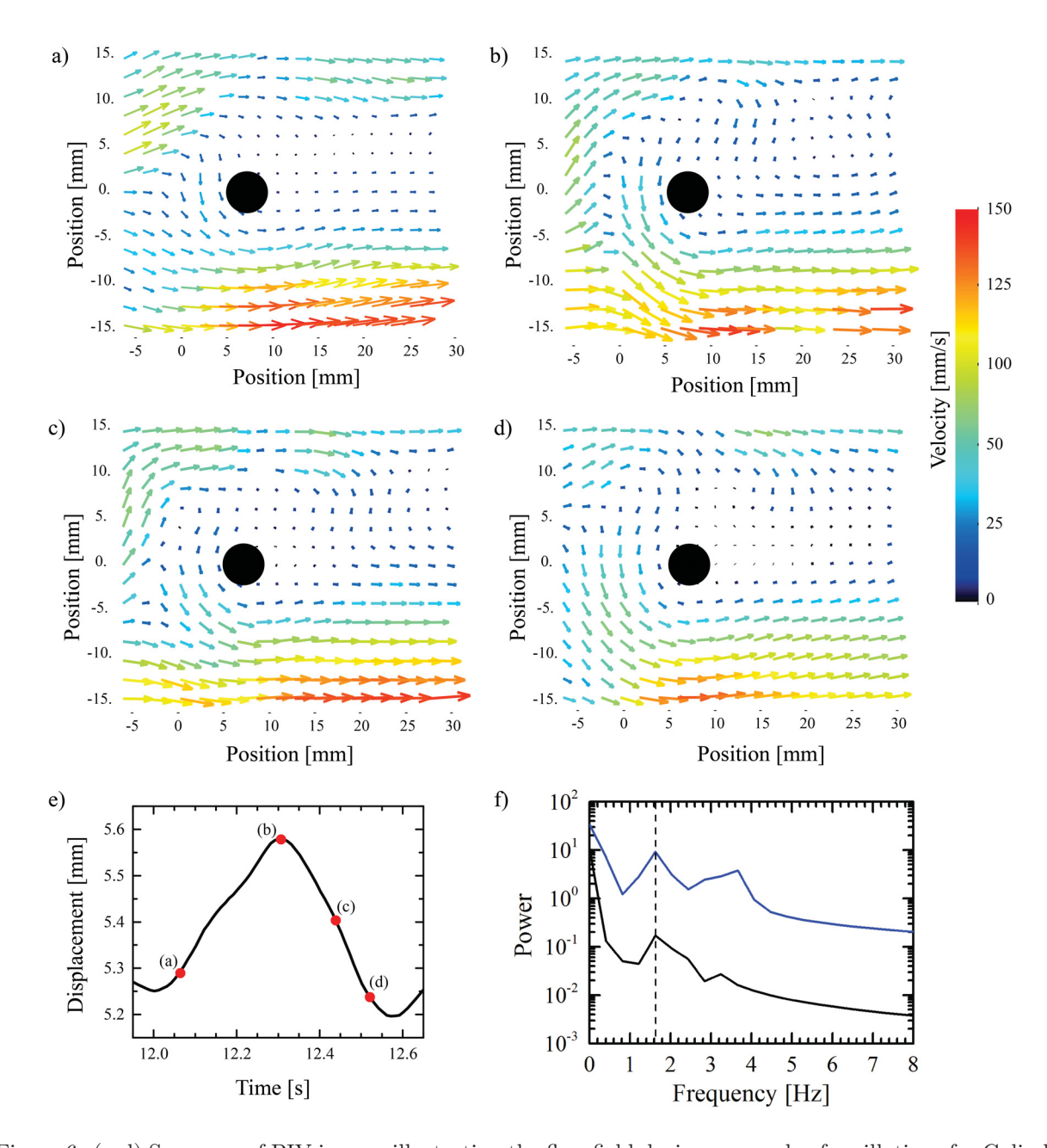


Figure 6: (a-d) Sequence of PIV images illustrating the flow field during one cycle of oscillations for Cylinder 1 at Wi=10 and $V_r=2.5$. The flow is from left to right. Each PIV image corresponds to a point highlighted in the time-history in (e). (f) The power spectra derived from the cylinder displacement (black) and fluctuating PIV velocity vectors (blue) within the reversed flow region occurring 20 mm downstream from the cylinder.

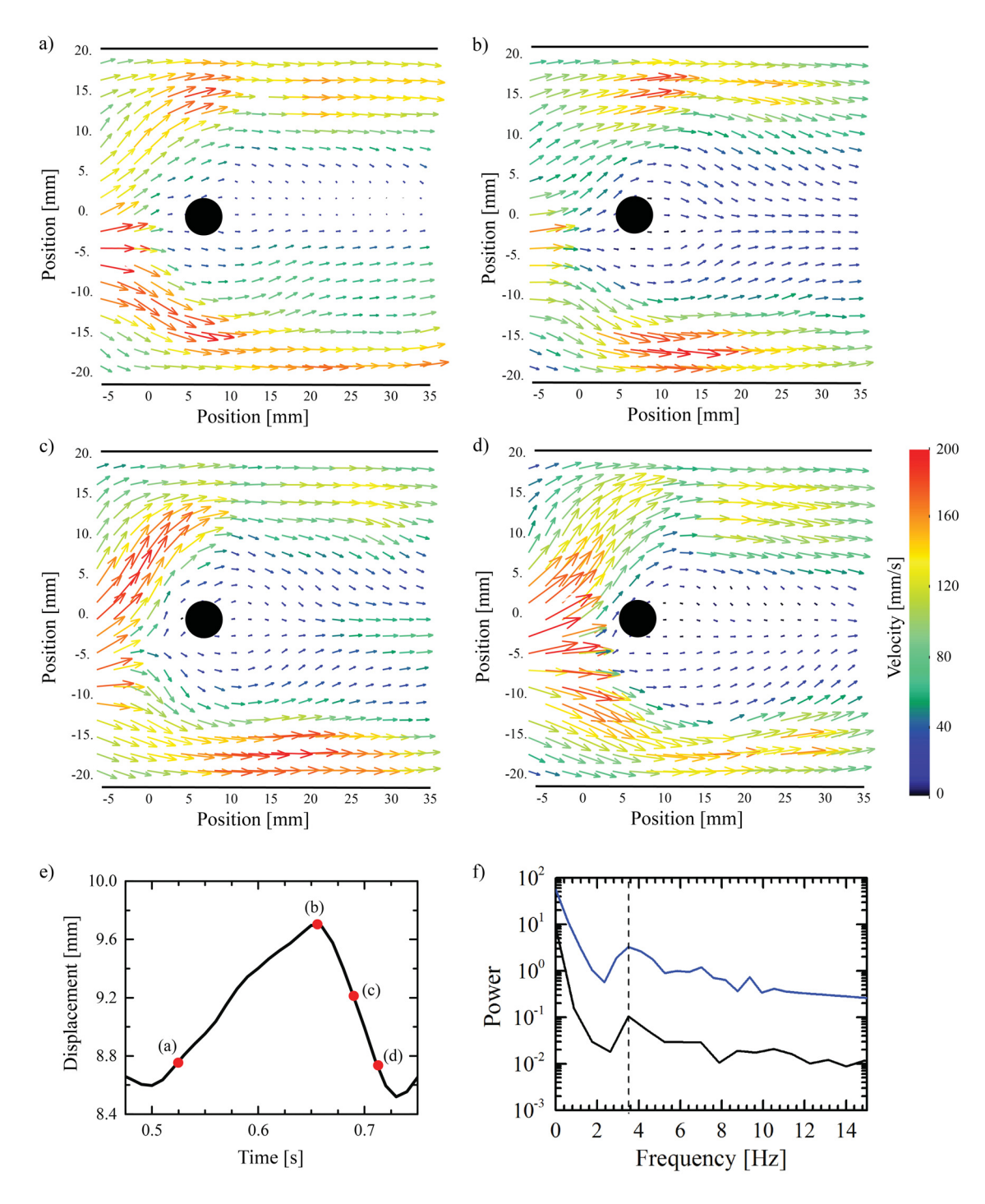


Figure 7: (a-d) Sequence of PIV images illustrating the flow field during one cycle of oscillations for Cylinder 1 at Wi = 24 and $V_r = 6$. The flow is from left to right. Each PIV image corresponds to a point highlighted in the time-history in (e). (f) The power spectra derived from the cylinder displacement (black) and fluctuating PIV velocity vectors (blue) located 20mm downstream in the wake of the cylinder centerline.

reversed flow only extends 1.5D downstream of the cylinder. Within the lock-in, however, the jet is significantly stronger and the reversed flow is more prevalent, extending 2.5D into the wake as seen in Fig. 6(c). The power spectra of the cylinder displacement and the fluctuating PIV velocity vectors within the region of reversed flow 20 mm downstream of the cylinder has been plotted against frequency in Fig. 6(f). During lock-in, the cylinder oscillation was observed to dynamically couple with the surrounding flow field as seen by the periodicity of the reversed flow downstream of the cylinder corresponding with the cylinder oscillation in Fig. 6(f).

When the Weissenberg number is increased further and the reduced velocity grows beyond the lock-in range, the flow pattern in the wake of the cylinder changes completely. This can be seen in Fig. 7 for a flow at Wi = 24 and $V_r = 6$. Here, the flow is nearly symmetric, and as seen in Fig. 7(b,c), the elastic flow instability still originates in the wake of the cylinder and produces a strong fluid jet several diameters downstream of the cylinder. The resulting cylinder oscillations are again driven by the wake instability as verified by the power spectra in Fig. 7(f) at these high Weissenberg numbers. However, during the cylinder oscillations, the flow remains largely symmetric and no flow reversal is observed at any point throughout the oscillation cycle. This distinct difference between the wake structure within and after the lock-in range clearly demonstrates the influence of the two-way coupling between the structure and the flow, as the motion of the cylinder clearly affects the flow pattern in the wake during the oscillations within the lock-in range and has little affect on the flow in the wake after the lock-in range.

4. Conclusions

We report the very first observation of lock-in during viscoelastic fluid-structure interactions between a flow of wormlike micelle solution and a flexibly-mounted cylinder, free to oscillate in the inline direction. Two flexibly-mounted cylinders of different natural frequencies were subjected to a flow of wormlike micelle solution. Beyond a critical Weissenberg number, the onset of flow instabilities in the wake of the cylinder triggered periodic cylinder oscillations. With increasing Weissenberg number, the frequency of cylinder oscillations increased and began to approach the natural frequency of the cylinder. At this point, a lock-in range was observed in which the frequency ratio stayed relatively constant, and slightly larger than 1. The amplitude of oscillations was also constant in the lock-in range. Lock-in was observed for a reduced velocity range of $1.5 < V_r < 4$. This range was completely covered by the data points from the experiments on Cylinder 1, but data points from Cylinder 2 covered only the beginning of the lock-in range, yet in both sets of experiments, the lock started at the same value of the reduced velocity.

The transient flow field during the oscillations of both cylinders were presented through PIV and streakline image sequences at various Weissenberg numbers and reduced velocities before, during and after the lock-in range. Before and after the lock-in range, both the frequency and amplitude of oscillations increased monotonically with increasing Weissenberg number and reduced velocity. The cylinder oscillations before and after lock-in were triggered due to elastic flow instabilities occurring in the wake of the cylinder similar to recent studies on FSI systems in viscoelastic fluids [10, 11, 12, 16, 17].

The flow field behavior during the lock-in was distinguished by an asymmetric region of reversed flow which appeared during the cylinder oscillations and extended deep into the wake of the cylinder. A synchronization between the appearance of this asymmetric reversed flow and cylinder oscillations was observed. Beyond lock-in, the reversed flow in the wake disappeared and the flow became more symmetric although still time dependent. These results are clearly different from the lock-in that is observed in the Newtonian cases where the oscillations exist only in the lock-in range and the cylinder does not oscillate when lock-in is not observed. These fundamental distinctions exist due to the complex relationship between the physical properties of a flexibly-mounted structure and the transient flow field occurring due to elastic instabilities of a viscoelastic fluid flow. The dynamic response of the structure during viscoelastic lock-in is influenced by the viscoelastic fluid rheology which in turn determines the onset frequency of the flow instabilities.

Acknowledgements

This work was funded by the National Science Foundation under grant CBET-1705251.

References

- [1] Anna, S.L., McKinley, G.H., 2001. Elasto-capillary thinning and breakup of model elastic liquids. Journal of Rheology 45, 115–138.
- [2] Bearman, P.W., 1984. Vortex shedding from oscillating bluff bodies. Annu. Rev. Fluid Mech. 16, 195–222.
- [3] Bhardwaj, A., Miller, E., Rothstein, J.P., 2007. Filament stretching and capillary breakup extensional rheometry measurements of viscoelastic wormlike micelle solutions. J. Rheol. 51, 693–719.
- [4] Cagney, N., Balabani, S., 2013a. Mode competition in streamwise-only vortex induced vibrations. Journal of Fluids and Structures 41, 156 165.
- [5] Cagney, N., Balabani, S., 2013b. On multiple manifestations of the second response branch in streamwise vortex-induced vibrations. Physics of Fluids 25, 075110.
- [6] Cagney, N., Balabani, S., 2013c. Wake modes of a cylinder undergoing free streamwise vortex-induced vibrations. Journal of Fluids and Structures 38, 127 145.
- [7] Cagney, N., Balabani, S., 2014. Streamwise vortex-induced vibrations of cylinders with one and two degrees of freedom. Journal of Fluid Mechanics 758, 702–727.
- [8] Chen, S., Rothstein, J.P., 2004. Flow of a wormlike micelle solution past a falling sphere. J. Non-Newtonian Fluid Mech. 116, 205 234.
- [9] Dahl, J., Hover, F., Triantafyllou, M., Oakley, O., 2010. Dual resonance in vortex-induced vibrations at subcritical and supercritical reynolds numbers. Journal of Fluid Mechanics 643, 395–424.

- [10] Dey, A.A., Modarres-Sadeghi, Y., Lindner, A., Rothstein, J.P., 2020. Oscillations of a cantilevered micro beam driven by a viscoelastic flow instability. Soft Matter, -.
- [11] Dey, A.A., Modarres-Sadeghi, Y., Rothstein, J.P., 2017. Experimental observation of viscoelastic fluid–structure interactions. Journal of Fluid Mechanics 813, R5.
- [12] Dey, A.A., Modarres-Sadeghi, Y., Rothstein, J.P., 2018. Viscoelastic fluid-structure interactions between a flexible cylinder and wormlike micelle solution. Phys. Rev. Fluids 3, 063301.
- [13] Gladden, J.R., Belmonte, A., 2007. Motion of a viscoelastic micellar fluid around a cylinder: Flow and fracture. Phys. Rev. Lett. 98, 224501.
- [14] Groisman, A., Steinberg, V., 2000. Elastic turbulence in a polymer solution flow. Nature 405, 53–55.
- [15] Gurian, T.D., Currier, T., Modarres-Sadeghi, Y., 2019. Flow force measurements and the wake transition in purely inline vortex-induced vibration of a circular cylinder. Phys. Rev. Fluids 4, 034701.
- [16] Haward, S.J., Kitajima, N., Toda-Peters, K., Takahashi, T., Shen, A.Q., 2019. Flow of wormlike micellar solutions around microfluidic cylinders with high aspect ratio and low blockage ratio. Soft Matter 15, 1927–1941.
- [17] Hopkins, C.C., A.Q., Purely elastic Haward, S.J., Shen, fluid-structure interactions microfluidics: Implications for mucocilin Small 16, 1903872. URL: https://onlinelibrary.wiley. iary flows. com/doi/abs/10.1002/smll.201903872, doi:10.1002/smll.201903872, arXiv:https://onlinelibrary.wiley.com/doi/pdf/10.1002/smll.201903872.
- [18] Israelachvili, J.N., 1985. Intermolecular and surface forces: with applications to colloidal and biological systems. Academic Press, London.
- [19] J. Appell, G. Porte, A. Khatory, F. Kern, S. J. Candau, 1992. Static and dynamic properties of a network of wormlike surfactant micelles (cetylpyridinium chlorate in sodium chlorate brine). J. Phys. II France 2, 1045–1052.
- [20] Khalak, A., Williamson, C., 1999. Motions, forces and mode transitions in vortex-induced vibrations at low mass-damping. J. Fluids Struct. 13, 813–851.
- [21] Larson, R., 1992. Instabilities in viscoelastic flows. Rheol. Acta 31, 213–263.
- [22] Larson, R.G., 1999. The Structure and Rheology of Complex Fluids. Oxford University Press, New York.
- [23] McKinley, G.H., Pakdel, P., Öztekin, A., 1996. Rheological and geometric scaling of purely elastic flow instabilities. J. Non-Newtonian Fluid Mech. 67, 19–47.
- [24] Mohammadigoushki, H., Muller, S.J., 2016. Sedimentation of a sphere in wormlike micellar fluids. Journal of Rheology 60, 587–601.

- [25] Moss, G.R., Rothstein, J.P., 2010a. Flow of wormlike micelle solutions past a confined circular cylinder. J. Non-Newtonian Fluid Mech. 165, 1505–1515.
- [26] Moss, G.R., Rothstein, J.P., 2010b. Flow of wormlike micelle solutions through a periodic array of cylinders. Journal of Non-Newtonian Fluid Mechanics 165, 1 13.
- [27] Rehage, H., Hoffmann, H., 1991. Viscoelastic surfactant solutions: model systems for rheological research. Mol. Phys. 74, 933–973.
- [28] Rothstein, J.P., 2003. Transient extensional rheology of wormlike micelle solutions. J. Rheol. 47, 1227–1247.
- [29] Sarpkaya, T., 2004. A critical review of the intrinsic nature of vortex-induced vibrations. J. Fluids and Struct. 19, 389 447.
- [30] Shaqfeh, E.S.G., 1996. Purely elastic instabilities in viscometric flows. Annu. Rev. Fluid Mech. 28, 129–185.
- [31] Williamson, C.H.K., Govardhan, R., 2004. Vortex-induced vibrations. Annu. Rev. Fluid Mech. 36, 413–455.